Applicability of Shockley-Read-Hall Theory for Interface States

Bernhard Ruch[*][†], Markus Jech[†], Gregor Pobegen[*] and Tibor Grasser[†]

[*]*KAI GmbH*, Villach, Austria, [†]*Institute for Microelectronics TU Wien*, Vienna, Austria

Abstract: Even though the Shockley Read Hall (SRH) model neglects atomic reconfiguration upon charge capture and emission, it has been successfully used for decades to describe the dynamics of interface states. This is quite in contrast to oxide bulk defects, where this omission results in serious modeling errors. Using ab initio models of dangling bonds at a model SiO_2/Si interface together with non-radiative multi-phonon theory, we explore why the SRH model gives excellent approximation in many cases and where its limits are.

Introduction: Investigations of the dynamics of interface traps often [1–3] employ Shockley-Read-Hall (SRH) theory [4] to model the transition dynamics between channel carriers and defects. A missing key feature of SRH theory is the structural change of the defects upon changes of its charge state. Using density functional theory (DFT) simulations, we identify three defects which reasonably resemble a P_b-center, the most probable defect [5] at the Si-SiO$_2$ interface. From these defects we extract the potential energy surfaces to describe the transitions in a standard non-radiative multi-phonon (NMP) model [6]. Using the more complete NMP model, we benchmark the SRH model against experimental spectroscopic charge pumping data and offer a justification for the often employed Arrhenius activated capture cross section introduced in the SRH model based on a simplification of the NMP model.

Microscopic Simulation of Interface Defects: Density functional theory simulations are performed with the CP2K package using 3D periodic boundary conditions in conjunction with the non-local functional PBE0_TC_LRC. Electrons are represented by a Gaussian basis with an auxiliary plane-wave basis set. In our case, a double-ζ basis set was used together with the Goedecker-Teter-Hutter pseudopotential with the plane wave cutoff set to 650 Ry. A reduction of the computational resources is achieved by employing the auxiliary density matrix method when processing the Hartree-Fock integrals of the nonlocal functional calculations. Additionally, further reduction of computational costs is possible by using a more sparse auxiliary basis set (pFIT) in addition to the main basis set. Geometry optimizations have been performed using the Broyden-Fletcher-Goldfarb-Shanno algorithm, thereby minimizing the forces on atoms to within 24 pN (Figs. 1, 2).

Over 100 3D periodic Si-SiO$_2$ interfaces with two interface regions were created using a melt and quench procedure with the classic force field ReaxFF [7–9]. The three most promising candidates for Si dangling bond (DB) defects, also known as P_b centers, were further optimized using DFT calculations and investigated in greater detail. Those particular Si-DB configurations resemble the well known geometrical characteristics of a Pb center; a trivalenty bonded Si atom with one unpaired electron in the vicinity of the Si-SiO$_2$ interface. Furthermore, they possess two charge transition levels, +/0 and 0/-, within the Si band gap (Fig. 3) – as expected for P_b centers [5, 10]. The first candidate, defect A (Fig. 4), is a Si atom one layer below the interface, trivalently bonded to three other Si atoms missing a fourth bond. Similarly, configuration B features a close-by O atom from the amorphous SiO$_2$ network. Lastly, defect C,

represents a Si-DB which is bonded to one O and two Si atoms. The spin densities visualized in Fig. 4 (translucent profiles) clearly show that the unpaired electron is fully localized on the respective defect configuration. The positively and negatively charged states of the defects are calculated in addition to the neutral state for the chosen configurations. Their structural reconfigurations are shown in Fig. 5. Generally, it is found that the silicon atoms do not significantly change their positions upon charge capture due to the rigid crystalline lattice. However, the a-SiO$_2$ structure is more flexible and considerable reconfigurations of nearby O atoms can be observed in B and partly C, which is particularly pronounced for the positive charge state.

Analytical Trap Models: Chargeable defects in oxides of semiconductor devices are usually separated into interface traps and oxide traps [11]. Interface traps are generally modeled by the Shockley-Read-Hall (SRH) model [4] which ignores configurational changes. For defects deeper within an oxide a more complete approach is always necessary: The non-radiative multi-phonon (NMP) model [6] considers spatial changes of the lattice induced by changes in the charge states of defects and can be used for the description of transition rates of charge carriers between the defects and a reservoir. Using the results of the above presented DFT simulations, we chose defect A to extract the parameters for an NMP investigation of interface traps to compare the NMP model, usually used for oxide defects, to the SRH model. The SRH energy barrier (Eq. (1) [6]) for emission transitions is equal to the energy difference between the equilibrium configurations in the two considered charge states (Fig. 6) and lacks any additional barriers. In the NMP model, the fact that transitions cause a change of the atomistic structures thereby requiring an additional relaxation energy (2) is considered. It can be extracted from the potentials of the defect states which are approximated as harmonic potentials (Eq. (3), Fig. 7) [6], where M is the effective mass of the 'defect molecule', ω_i the vibrational frequency in the minimum i, Δq the difference between the reaction coordinate and the local equilibrium position, and E_i the potential energy in the minimum. A quadratic fit of the potential for the charged states assuming linear electron-photon coupling ($\omega_i=\omega$ for all i) yields (2) and leads to the energetic barrier for emission transitions in the NMP model (4). From our DFT simulations we extract relaxation energies for the charged states. The positively charged state has an ε_R of 0.215 eV, the negatively charged state an ε_R of 0.179 eV. Capture transitions for both models can be obtained by (5). In the following, the derivation will focus on holes, i.e. electron interactions with the valence band ($E_{21} = E_t - E_V$), as the conduction band interactions can be described completely analogously. Using the transition barriers for the SRH and NMP models, the hole capture transition rate is given by (6). Similarly, the hole emission transition rate is written as (7).

Experimental Structures and Measurement Procedure: We investigated the behavior of interface defects on lateral n-channel MOSFETs with a channel length of 6 μm, a channel width of 100 μm, and a 30 nm SiO$_2$ insulator. These devices are surrounded by a poly-crystalline silicon heater (poly-heater), which is used to regulate the device temperature by Joule-heating. This is achieved by cooling the structure to a base

temperature of -60 °C and applying a pre-calibrated bias to the poly-heater, thereby reaching arbitrary temperatures up to approximately 200 °C [12]. All measurements were performed on wafer-level, where a temperature controlled chuck cools the whole wafer to the base temperature. Traps are generated by a 20 ks hot-carrier stress (V_D=8 V, V_G=4 V) at various stress temperatures allowing for a quantitative adjustment of the hot-carrier stress generated traps, as HCD is strongly temperature dependent [13]. Regular and spectroscopic charge pumping (SPCP) [14] was chosen as the main defect characterization method to obtain density of state spectra of interface traps in the band gap. Due to the wide temperature range of this measurement method, compared to other CP methods, the SRH theory can be tested thoroughly as a function of temperature. Generally, the MOS structure under investigation is pulsed from deep inversion to deep accumulation in all charge pumping methods [15]. Defects capturing carriers during the accumulation phase re-emit them during the inversion phase and vice versa. This leads to a measurable net current I_{CP} between the n- and p-doped areas near or under the MOS structure, which is in our case between the tied drain and source contacts and the body contact. A parasitic effect of CP, the emission of carriers during the phase in which they are captured, is dependent on the emission time constants of the traps. Thus, rise and fall times of the slopes of the applied pulse regulate this parasitic effect. SPCP makes use of this effect by sweeping the rise and fall times of the pulses to energetically scan the band gap [1]. Later, the rise and fall time sweeps can be transformed into the energetic component of the spectrum while the change of the CP current is transformed into the density of states. It is noted that the inverse of the transition rates for emission (8) is related to the rise time of SPCP: The fraction of the rise time of the CP pulse with an amplitude of ΔV_g which transitions between the threshold voltage and flat-band voltage of CP (V_{TH}^{CP} and V_{FB}^{CP}) is assumed to be equal to the emission time constant τ_{em}^{h+} [1]. This assumption is based on the idea that emission is only possible when the channel area is neither in inversion nor accumulation. Thus, the energy transformations of the density of states in SPCP (9) and (10) can be obtained from (1) for the SRH model or (4) for the NMP model, respectively, using (8). At this point, a bridge between the SRH and NMP models can be built assuming energy differences between defects and reservoir which are significantly larger than relaxation energies ($E_{21} \gg \varepsilon_R$). This yields $\varepsilon_{21}^{NMP} \approx \varepsilon_R/4 + E_{21}$ which leads to the commonly used Arrhenius correction (11) of capture cross sections [16]. This NMP capture cross section (Eq. (11)) can be used in (9) to obtain the energy transformation of the SRH model with temperature compensation (SRHT) (12). Interestingly, this adds an offset $-\varepsilon_R/4$ to the SRH energies similarly to the $-\varepsilon_R$ offset observed in the NMP energies. The transformation of the CP current to the density of states (13) [1] leads to the same spectra for the SRH and SRHT models (14) known from SPCP literature but a new result for the NMP model, namely (15).

Results and Discussion: Fig. 8 shows the temperature dependence of the trap energies for a given emission time constant for both valence and conduction band interactions. This reflects the maximum possible energy window of CP and SPCP between the respective curves for each model. If we take the most complete NMP model as the benchmark, the SRH model performs worse than the SRHT model, which is not surprising given that the SRHT model considers the relaxation energy in the capture cross section. Capture and emission rate ((6) and

(7)) dependencies over the Fermi level can easily be compared for the three models (NMP, SRH, SRHT), cf. Fig. 9, where the capture rates are constant over the Fermi level as they are independent of the carrier concentration. Neither the SRH nor the SRHT model are able to perfectly map the NMP model. This imperfection of modeling does not bother us unduly since trap energies of the SRH and SRHT model match well to the NMP model. A direct comparison of the NMP trap energies to SRH and SRHT trap energies is depicted in Fig.10 for various measurement temperatures. It is found that the SRHT model hardly deviates from the NMP calculations. However, the SRH model, while performing worse, does not deviate too much either. In order to compare the models to real measurement data, it is necessary to find the correct capture cross section for the analysis with the three models. Therefore, the trap density of SPCP N_{spec} obtained from the integration over the $D(E)$ spectrum was compared to the trap density of standard CP N_{std} (Fig. 11) which is proportional to I_{CP} and thus independent of trap models. The integration of $D(E)$ was performed for varying capture cross sections and four measurements. For improved readability, only one measurement for each model is shown in Fig. 11. From the intersection of the integrated spectra with the standard CP trap value for the respective measurement, the capture cross section can be extracted. This analysis yielded $\sigma_{NMP} = 2.0 \pm 1.3 \times 10^{-16}$ cm^2 for the NMP model, $\sigma_{SRH} = 14 \pm 9.0 \times 10^{-16}$ cm^2 for the SRH model and $\sigma_{SRH} = 5.7 \pm 4.3 \times 10^{-16}$ cm^2 for the SRHT model. As predicted by our calculations, the cross sections of the SRH and SRHT models overlapped confirming the validity of assumption (11). The impact of the models on the spectra evaluation of SPCP is presented in Fig. 12 for one measurement: As already observed in earlier analytical calculations, the SRH model again deviates slightly from the NMP model while the SRHT model is able to predict the energetic positions of the spectrum with respect to the NMP model very well. The SRHT model only corrects the energetic distribution, though, and lacks an adjustment of the values of the density of states due to structural relaxations which are considered in the NMP model. When integrating the spectra of various measurements at different stress temperatures and comparing the resulting trap densities to standard CP as shown in Fig. 13, taking the variance of the capture cross sections into account, almost no difference in the models can be observed. This indicates that, in this kind of analysis, the deviations of the different models is averaged out by the integration.

Conclusion: Using molecular configurations of P$_b$ centers from DFT simulations we calculated the structural relaxation resulting upon charge capture. With the NMP model, which considers the structural changes near and on the Si-oxide interface, as a benchmark, we were able to show the limitations of the SRH model. It is possible to improve the SRH model by using an Arrhenius activated capture cross section, which was shown to be equivalent to a simplification of the NMP model. All three models are compared for a data set obtained by CP and SPCP. From this comparison, we conclude that the SRH model is an adequately good approximation of the NMP model, which can be vastly improved by a temperature dependent σ. The relatively small structural relaxation compared to oxide defects is the primary reason SRH could be used for such a long time to describe interface states without major issues. Also, the temperature dependence of defects is often not, or only over a small range, investigated. Thus, temperature dependent effects may be concealed by an adjustment of the capture cross section.
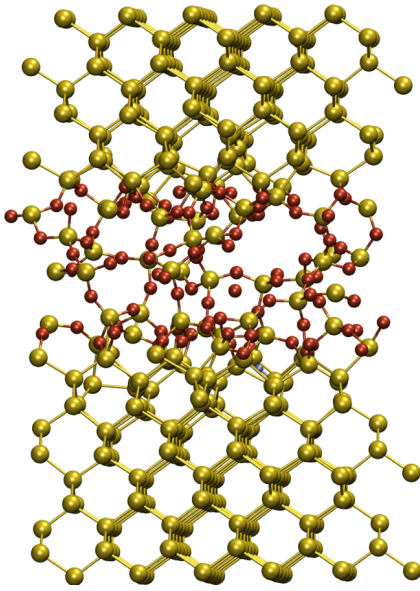
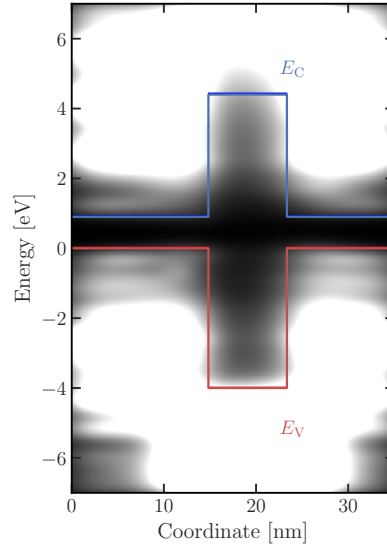Fig. 1. Example of a Si-SiO$_2$-Si structure used in the DFT calculation.

Fig. 2. Conduction and valence bands obtained from a DFT simulation of the interface model shown in Fig. 1 containing around 500 atoms. The known band gaps of Si and SiO2 are well represented by the calculations which yield E$_{g,Si}$ = 1.0 eV and E$_{g,SiO_2}$ = 8.7 eV, respectively.
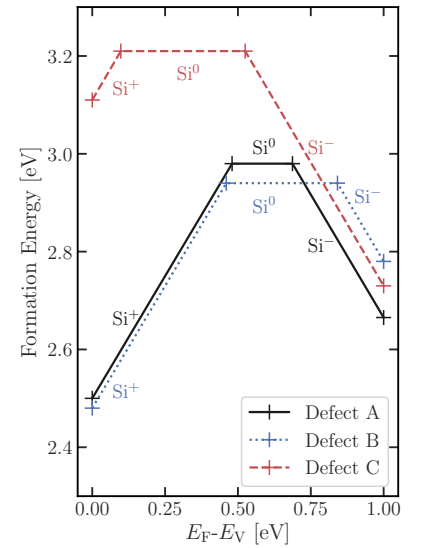

Fig. 3. Formation energies of the defects A, B and C plotted over the Fermi level with respect to the valance band of Si for the three possible charge states.
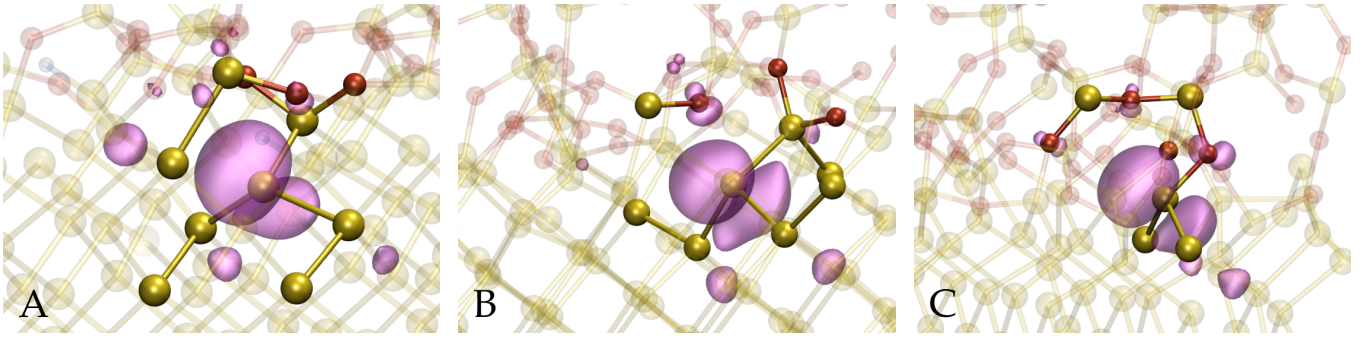
Fig. 4. Spin density of the defects A, B and C (left to right). Si atoms are represented in yellow, O atoms in red. Defect A and B both miss a forth Si atom in the lattice while there are no O atoms in the vicinity of A in contrast to B. In defect C, a Si-DB is bonded to one O atom and two Si atoms. Isosurfaces of 0.01 in violet.
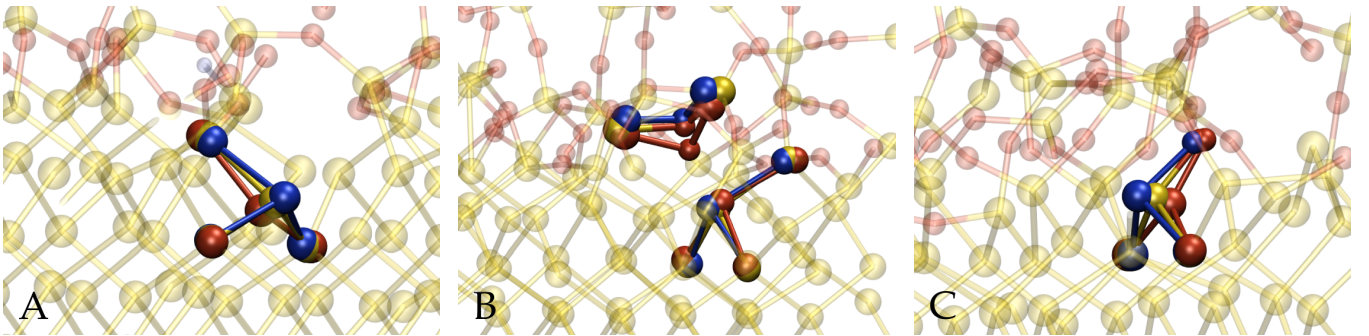

Fig. 5. Structural reconfiguration of the defects A, B and C (left to right) when positively (red), negatively (blue) or neutrally (yellow) charged.

[1] T. Aichinger and M. Nelhiebel. *IEEE TDMR* 8.3 (2008), pp. 509–518. [2] T. Tsuchiya. *APE* 4.9 (2011), p. 094104. [3] P. Masson et al. *APL* 81.18 (2002), pp. 3392–3394. [4] W. Shockley and W. T. Read. *Phys. Rev.* 87.5 (1952), pp. 835–842. [5] L.-A. Ragnarsson and P. Lundgren. *JAP* 88.2 (2000), pp. 938–942. [6] T. Grasser. *Micro. Rel.* 52.1 (2012), pp. 39–70. [7] M. Jech et al. *Phys. Rev. B* 100 (19 2019), p. 195302. [8] Fogarty et al. *J. Chem. Phys.* 132.17 (2010), p. 174704. [9] Aktulga et al. *Parallel Computing* 38.4 (2012), pp. 245–259. [10] A. Stesmans. *PRB* 48 (4 July 1993), pp. 2418–2435. [11] D. M. Fleetwood. *IEEE Trans. Nucl. Sci.* 39.2 (Apr. 1992), pp. 269–271. [12] G. Pobegen et al. *IEEE TDMR* 14.1 (2014), pp. 169–176. [13] F. Hsu and K. Chiu. *IEEE EDL* 5.5 (1984), pp. 148–150. [14] G. Van den Bosch et al. *IEEE TED* 38.8 (1991), pp. 1820–1831. [15] G. Groeseneken et al. *IEEE TED* 31.1 (1984), pp. 42–53. [16] M. J. Kirton and M. J. Uren. *APL* 48.19 (1986), pp. 1270–1272.
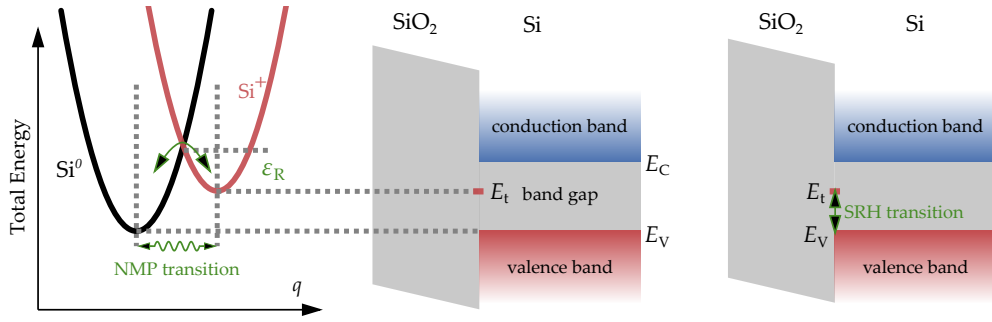
Fig. 6. Comparison of NMP and SRH transitions for holes. NMP transitions consider the barrier between the two states caused by the relaxation energy. Structural relaxation is ignored in the SRH model and only the energy difference between the two states is considered. SRH transitions are direct and lack the relaxation energy ε_R barrier present in the NMP model.
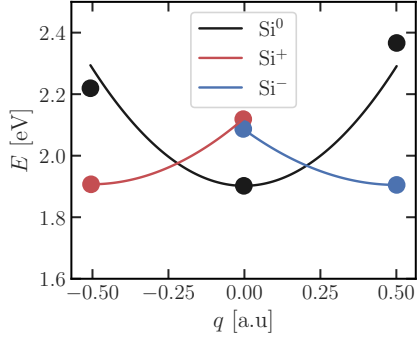

Fig. 7. Total energy of defect A for neutral, positive and negative charge states over the reaction coordinate q obtained from DFT simulations. Fit with parabolas in order to extract relaxation energies.
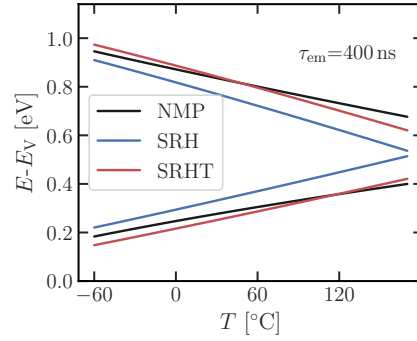
Fig. 8. Temperature dependence of the energetic limits of CP for the NMP, SRH and SRHT models for a constant value of τ_{em}.
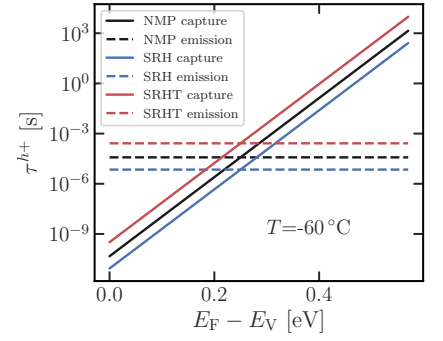
Fig. 9. Comparison of the capture and emission times for NMP, SRH and SRHT models.
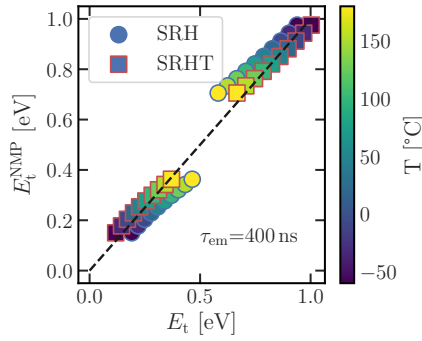

Fig. 10. Comparison of the trap energies in SPCP obtained from the SRH and SRHT models to the trap energies from the NMP model.
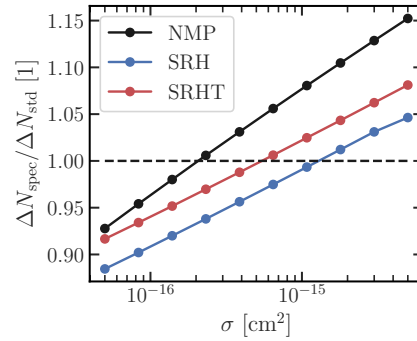
Fig. 11. Extraction method for the capture cross section σ obtained by comparison of integrated $D(E_t)$) spectra and standard CP.
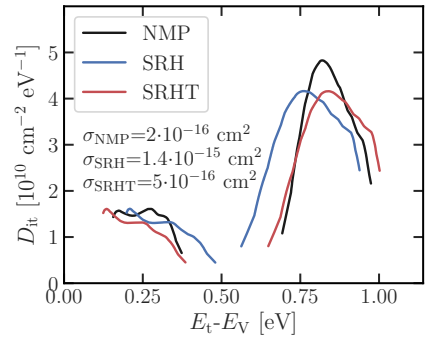
Fig. 12. Comparison of $D(E)$ spectra of SPCP obtained from the NMP, SRH and SRHT models for a single raw data set of SPCP data.
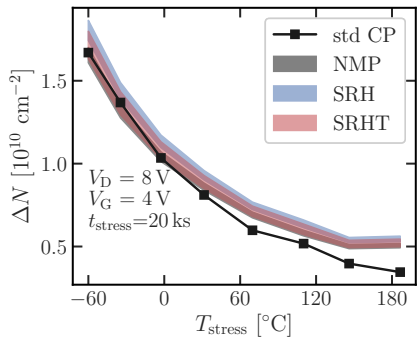

Fig. 13. Comparison of integrated $D(E)$ trap densities and trap densities of standard CP after a hot-carrier stress, where $D(E)$ was obtained from NMP, SRH and SRHT models. Stress dose varied by changing the temperature during stress.

$$\varepsilon_{21}^{SRH} = E_{21} \tag{1}$$

$$\varepsilon_R = \frac{1}{2} M \omega_i^2 \Delta q^2 \tag{2}$$

$$V_i = \frac{1}{2} M \omega_i^2 \Delta q^2 + E_i \tag{3}$$

$$\varepsilon_{21}^{NMP} = \frac{(\varepsilon_R - E_{21})^2}{4\varepsilon_R}$$
$$= \frac{\varepsilon_R}{4} + \frac{E_{21}^2}{4\varepsilon_R} - \frac{E_{21}}{2} \tag{4}$$

$$\varepsilon_{12} = \varepsilon_{21} + E_{21} \tag{5}$$

$$k_{12}^{h+} = p v_{th} \sigma \exp\left(-\frac{\varepsilon_{12}}{k_B T}\right) \tag{6}$$

$$k_{21}^{h+} = N_V v_{th} \sigma \exp\left(-\frac{\varepsilon_{21}}{k_B T}\right) \tag{7}$$

$$\tau_{em}^{h+} = \frac{1}{k_{21}^{h+}} = \frac{|V_{TH}^{CP} - V_{FB}^{CP}|}{\Delta V_g} t_r \tag{8}$$

$$-E_{21}^{SRH} = k_B T \ln\left(\tau_{em}^{h+} N_V v_{th} \sigma^{SRH}\right) \tag{9}$$

$$-E_{21}^{NMP} + \varepsilon_R^{h+} = \sqrt{4\varepsilon_R^{h+} k_B T \ln\left(\tau_{em}^{h+} N_V v_{th} \sigma^{NMP}\right)} \tag{10}$$

$$\sigma_{NMP} \approx \sigma_{SRH} \exp\left(-\frac{\varepsilon_R}{4 k_B T}\right) \tag{11}$$

$$-E_{21}^{SRHT} + \frac{\varepsilon_R^{h+}}{4} = k_B T \ln\left(\tau_{em}^{h+} N_V v_{th} \sigma^{SRH}\right) \tag{12}$$

$$\frac{dI_{CP}}{dt_r} = qAf D(E_t(t_r)) \frac{dE_t}{dt_r} \tag{13}$$

$$D(E_t(t_r))^{SRH} = \frac{dI_{CP}}{dt_r} \frac{t_r}{qAf} \frac{1}{k_B T} \tag{14}$$

$$D(E_t(t_r))^{NMP} = \frac{dI_{CP}}{dt_r} \frac{t_r}{qAf} \sqrt{\frac{\ln\left(\tau_{em}^{h+} N_V v_{th} \sigma^{NMP}\right)}{\varepsilon_R^{h+} k_B T}} \tag{15}$$

Fig. 14. Left: Equations describing the dynamics of SRH and NMP transitions. Right: Equations for the transformation of measured parameters of SPCP into spectra using the NMP, SRH and SRHT models.